



ELSEVIER

Contents lists available at ScienceDirect

## Planetary and Space Science

journal homepage: [www.elsevier.com/locate/pss](http://www.elsevier.com/locate/pss)

## 3D-modeling of Mercury's solar wind sputtered surface-exosphere environment

M. Pflieger<sup>a</sup>, H.I.M. Lichtenegger<sup>a,\*</sup>, P. Wurz<sup>b</sup>, H. Lammer<sup>a</sup>, E. Kallio<sup>c</sup>, M. Alho<sup>c</sup>, A. Mura<sup>e</sup>, S. McKenna-Lawlor<sup>f</sup>, J.A. Martín-Fernández<sup>d</sup><sup>a</sup> Space Research Institute, Austrian Academy of Sciences, Schmiedlstraße 6, A-8042 Graz, Austria<sup>b</sup> Physikalisches Institut, University of Bern, Sidlerstraße 5, CH-3012 Bern, Switzerland<sup>c</sup> Aalto University, School of Electrical Engineering, Helsinki, Finland<sup>d</sup> Department for Computer Science and Applied Mathematics, University of Girona, Edifici P-IV, Campus Montilivi, E-17071 Girona, Spain<sup>e</sup> Istituto Nazionale Di Astrofisica, Viale del Parco Mellini n°84, 00136 Roma, Italy<sup>f</sup> National University of Ireland, Maynooth, Ireland

## ARTICLE INFO

## Article history:

Received 4 September 2014

Received in revised form

24 April 2015

Accepted 28 April 2015

Available online 9 May 2015

## Keywords:

Mercury

Messenger

BepiColombo

Surface sputtering

Exosphere

Particle release

## ABSTRACT

The efficiency of sputtered refractory elements by  $H^+$  and  $He^{++}$  solar wind ions from Mercury's surface and their contribution to the exosphere are studied for various solar wind conditions. A 3D solar wind–planetary interaction hybrid model is used for the evaluation of precipitation maps of the sputter agents on Mercury's surface. By assuming a global mineralogical surface composition, the related sputter yields are calculated by means of the 2013 SRIM code and are coupled with a 3D exosphere model. Because of Mercury's magnetic field, for quiet and nominal solar wind conditions the plasma can only precipitate around the polar areas, while for extreme solar events (fast solar wind, coronal mass ejections, interplanetary magnetic clouds) the solar wind plasma has access to the entire dayside. In that case the release of particles from the planet's surface can result in an exosphere density increase of more than one order of magnitude. The corresponding escape rates are also about an order of magnitude higher. Moreover, the amount of  $He^{++}$  ions in the precipitating solar plasma flow enhances also the release of sputtered elements from the surface in the exosphere. A comparison of our model results with MESSENGER observations of sputtered Mg and Ca elements in the exosphere shows a reasonable quantitative agreement.

© 2015 Elsevier Ltd. All rights reserved.

## 1. Introduction

In the tenuous exosphere of Mercury a number of different species have been detected up to now: H, He, O, Na, Ca, K (e.g. Killen et al., 2007) and – more recently – Mg (McClintock et al., 2009). The total surface pressure of these species is  $\sim 10^{-12}$  mbar and is about two orders of magnitude lower than the derived upper limit of the exospheric pressure of  $\sim 10^{-10}$  mbar (Fjeldbo et al., 1976; Hunten et al., 1988). Hence some additional yet unobserved volatile material may populate the Hermean exosphere.

There is good reason to consider the solar wind and magnetospheric plasma precipitation onto the surface of Mercury to contribute to the population of the exosphere by ion implantation and sputtering processes. Numerical modeling of Mercury's magnetosphere has shown that the weak intrinsic magnetic field of the

planet is sufficient to prevent the equatorial regions from being impacted by solar wind ions during moderate solar wind conditions (Kallio and Janhunen, 2004). However, intense fluxes of protons are expected to hit the surface at high northern and southern latitudes, the auroral regions, giving rise to the release of surface elements at high latitudes by ion sputtering. During extremely high solar wind dynamic pressure conditions, the solar wind ions will have access to the entire dayside surface of Mercury (Slavin et al., 2014), which may result in a considerable increase in the particle population of the exosphere by sputtered material from Mercury's surface.

Ground-based observations of Mercury's surface can only provide averages of its mineralogical composition over a large area on the surface due to the limited spatial resolution because of atmospheric disturbances (Sprague et al., 2007). Recent measurements of the x-ray and gamma-ray spectrometers aboard the MErcury Surface, Space Environment, GEochemistry, and Ranging (MESSENGER) spacecraft acquired at different localized areas

\* Corresponding author.

E-mail address: [herbert.lichtenegger@oeaw.ac.at](mailto:herbert.lichtenegger@oeaw.ac.at) (H.I.M. Lichtenegger).

allowed to estimate the abundances of some elements like Si, Mg, S, Fe, Ti, and Al. Relatively high Mg/Si and S/Si ratios have been found, while Al/Si, Ca/Si, Fe/Si and Ti/Si ratios appear to be low (Nittler et al., 2011; Rhodes et al., 2011; Evans et al., 2012; Starr et al., 2012). Moreover, comparison of the x- and gamma-ray observations indicate that Mercury's regolith is on average vertically homogenous to a depth of tens of centimeters (Evans et al., 2012).

In this paper we consider only refractory elements that are ejected into the exosphere via solar wind sputtering. Therefore, the contribution of volatile elements like sodium or potassium to the exospheric composition is not considered in the present study. For refractory elements, release processes like electron and photon stimulating desorption are expected to be of minor importance. Also thermal desorption may contribute to the exosphere density at most close to the surface of Mercury. Micro-meteorite impact vaporization may result in a surface density comparable to that of sputtering, depending on the assumed impact flux. The initial ejecta can be described by a high-temperature vapor (~4000 K) allowing only a small fraction of non-volatile material to reach higher altitudes and to escape (Killen et al., 2007).

The Hermean environment is a complex system immersed in the solar wind, consisting of a surface-bounded exosphere containing volatile and refractory species from the regolith and interplanetary dust. We are not attempting to describe this dynamic system in detail, rather we are aiming to establish a global model of Mercury's exosphere. For this purpose we start with a plausible mineralogical model of the surface consistent with recent observations and consider the precipitation of solar wind ions onto the surface of Mercury for different solar wind conditions. By means of the corresponding sputter rates the 3-dimensional exosphere density of the sputtered species can be estimated and a self-consistent model of the expected average neutral particle environment of Mercury is obtained.

The paper is structured as follows: Section 2 describes the numerical models used, including the solar wind precipitation (Section 2.1), Mercury's elemental surface composition model (Section 2.2), the resulting sputter flux (Section 2.3), and the exosphere model (Section 2.4). Section 3 discusses the simulation results, while the conclusions are outlined in Section 4.

## 2. Model description

The sputter contribution to Mercury's exosphere is considered as the result of three major physical processes: (a) precipitation of solar wind ions, i.e., mainly  $H^+$  and  $He^{++}$  ions, (b) sputtering of surface elements, and (c) spreading of the sputtered particles around the planet.

### 2.1. Solar wind precipitation

The precipitating solar wind particles ( $H^+$  and  $He^{++}$  ions) are collected at the surface of Mercury, i.e., when absorbed by the obstacle, after the initial transients in the simulation have disappeared. The simulated particles are binned to a  $30 \times 30$  rectangular latitude–longitude grid by species, from which the corresponding fluxes are obtained from a three dimensional self-consistent Mercury hybrid model simulation (HYB-Mercury). In the hybrid model ions are treated as particles while electrons form a massless charge neutralizing fluid (Kallio and Janhunen, 2003a). Earlier HYB-Mercury runs made before MESSENGER observations modeled the Hermean magnetic field by using a magnetic dipole at the center of the planet, which gave a 300 nT magnetic field at the equator at the surface (Kallio and Janhunen, 2003a,b, 2004). However, the MESSENGER magnetic field observations indicated a  $195 \pm 10$  nT dipole field, which has an offset of  $484 \pm 11$  km

**Table 1**

Vectors components  $\vec{B}_{IMF} = (B_x, B_y, B_z)$  of the IMF ( $x$  parallel to solar wind flow direction,  $z$  parallel to magnetic dipole moment and  $y$  completes the right handed coordinate system), solar wind bulk velocity  $v_{bulk}$ , solar wind density  $n_{sw}$ , solar wind dynamic pressure  $P_{sw}$ , and fraction  $x_{He}$  of  $He^{++}$  ions in the solar wind for four considered cases.

	$\vec{B}_{IMF}$ (nT)	$v_{bulk}$ (km s <sup>-1</sup> )	$n_{sw}$ (cm <sup>-3</sup> )	$P_{sw}$ (nPa)	$x_{He}$ (%)
Case 1	(12.9, 4.7, 10.3)	400	60	15.9	5
Case 2	(0, 0, 15)	400	60	15.9	5
Case 3	(26.9,20)	350	90	18.3	8
Case 4	(26.9,20)	1200	90	215.2	8

northward of the geographic equator (Anderson et al., 2011). Some later studies suggested a 190 nT dipole field (Johnson et al., 2012). In this study the magnetic field of Mercury is modeled in the HYB-Mercury simulation as a dipole, with the dipole source translated 450 km northwards from the center of the planet, with a strength of 190 nT at the magnetic equator at Mercury's surface.

In Table 1 the interplanetary magnetic field (IMF) and solar wind conditions for four different cases used in the present simulations are summarized. Case 1 is intended to simulate 'mean' near-Mercury conditions similar to those measured during the first Mercury flyby (M1) of MESSENGER (Baker et al., 2009, 2011; Slavin et al., 2010), case 2 considers a northward directed IMF, and cases 3 and 4 represent solar wind conditions with a stronger IMF and higher solar wind density. Additionally, case 4 corresponds to a very high bulk speed. MESSENGER observations of Mercury's dayside magnetosphere under extreme solar wind conditions have been reported by Slavin et al. (2014). Of the three events analyzed, two were the result of coronal mass ejections and one was from a high speed stream, with inferred ram pressures of ~45 to 65 nPa. Case 4 can thus be considered as an example of even more extreme conditions than those observed by Slavin et al. (2014). The calculated solar wind flux onto Mercury's surface for all four cases is illustrated in Fig. 1.

### 2.2. Mercury's surface composition

As outlined in Wurz et al. (2010) – besides disk-averaged spectra from the first MESSENGER flyby and spatially resolved observations from the Mercury Atmospheric and Surface Composition Spectrometer (MASCS) instrument (McClintock et al., 2008) – the main knowledge of Mercury's global average surface composition is mainly inferred from ground-based observations in the visible and IR spectral ranges, as well as from experiments with analogue materials in laboratories (Warell et al., 2006; Sprague et al., 2007, 2009; Wurz et al., 2010). However, ground-based measurements of Mercury's surface mineralogy are hampered by various circumstances like the absorption features of the terrestrial atmosphere in the infrared wavelength range or the planet's closeness to the Sun. Furthermore, Mercury's surface has experienced space weathering for more than 4 billion years (Hapke, 2001) resulting in a substantial regolith layer, which makes the spectroscopic identification of minerals on the surface difficult.

Based on this available spectroscopic observations regarding the mineralogical information of Mercury's surface, Wurz et al. (2010) designed a global mineralogical model of the planet's elemental surface composition. This surface composition model consists of a selected group of end-member mineral compositions (~27 mol% feldspar, ~32 mol% pyroxene, ~39 mol% olivine, ~0.07 mol% metallic iron and nickel, ~1.03 mol% sulfides, ~0.07 mol% ilmenite, ~1.45 mol% apatite), which are weighted to be consistent with the available observational constraints and yields an average surface density of  $\sim 3.11$  g cm<sup>-3</sup>. From this

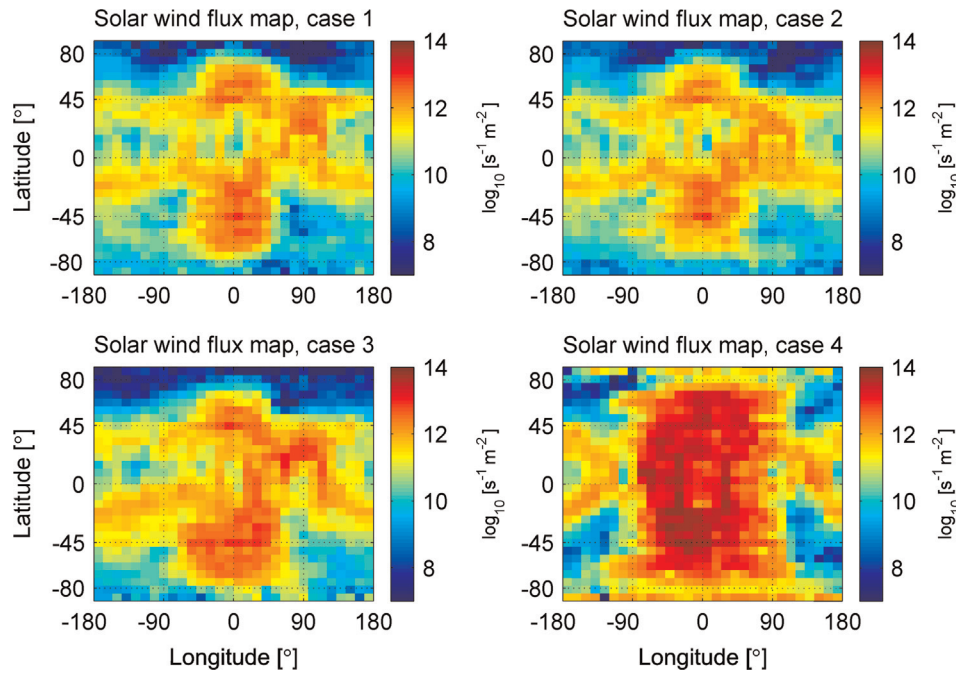


**Fig. 1.** Solar wind flux maps of precipitating  $H^+$  and  $He^{++}$  ions onto Mercury's surface in units of  $s^{-1} m^{-2}$  for four different cases varying in the strength of the IMF, the solar wind bulk velocity  $v_{bulk}$ , the solar wind density ( $H^+$  and  $He^{++}$  ions)  $n_{sw}$  and the helium fraction  $x_{He}$  (see Table 1). The subsolar point lies in the center of the maps, positive latitudes correspond to Mercury's northern hemisphere, positive longitudes represent the eastern hemisphere.

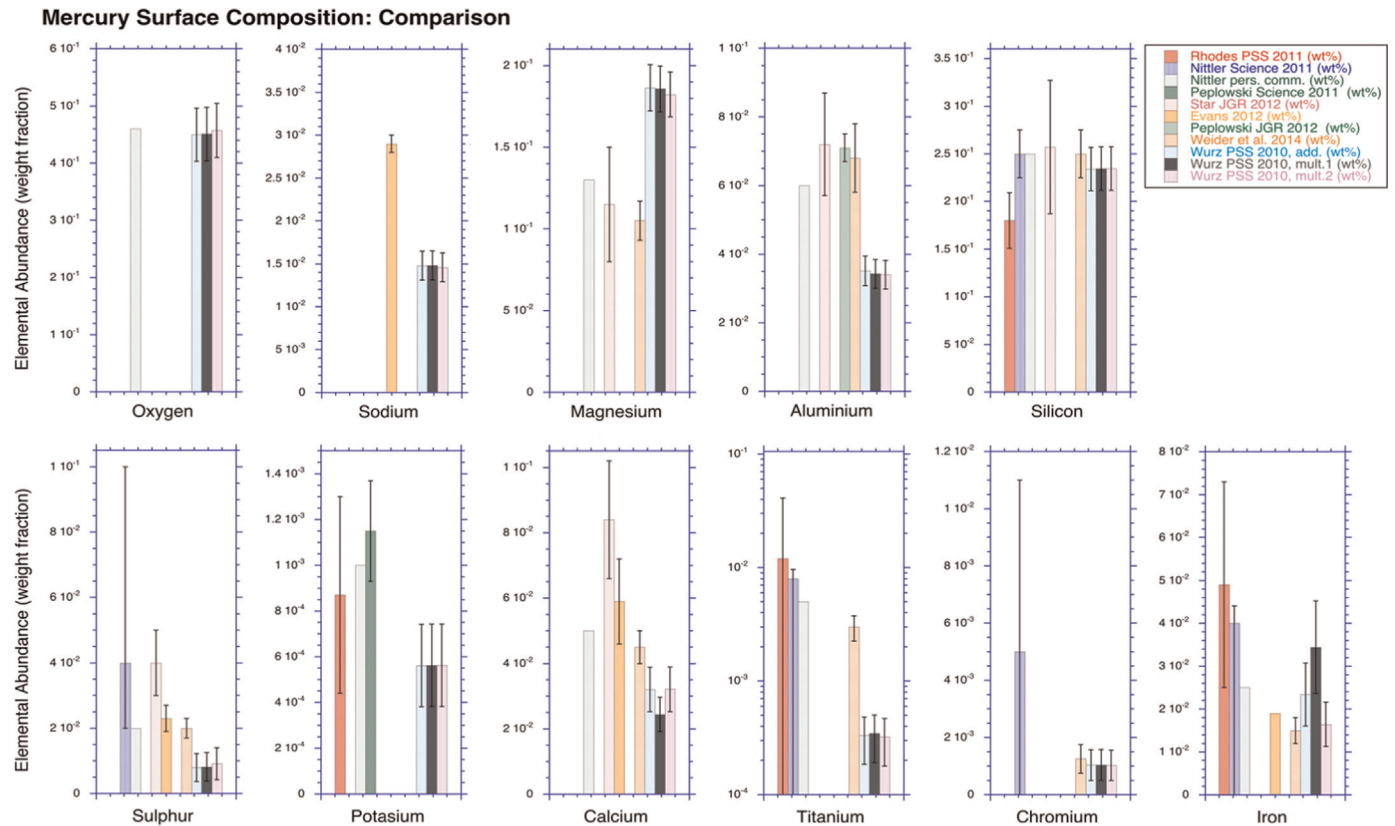


**Fig. 2.** Comparison of several measurements of the elemental surface compositions together with the predicted composition in units of weight percent.

mineralogical model Wurz et al. (2010) obtained the elemental composition of Mercury's surface by applying additive and multiplicative surface composition modeling techniques. Additionally they applied the multiplicative model with an assumed invariant Ca fraction of 1.67 % to better reproduce ground-based Ca exosphere observations (Bida et al., 2000).

The elemental fractions given in Wurz et al. (2010) have been converted to weight fractions to allow comparison with the published data from the MESSENGER mission (Nittler et al., 2011; Rhodes et al., 2011; Peplowski et al., 2011, 2012; Starr et al., 2012; Weider et al., 2012). As can be seen from Fig. 2, the predicted abundances of most of the elements compare reasonably well with

**Table 2**

Elemental surface abundance in units of atom percent as modeled with the multiplicative composition modeling technique with a fixed Ca fraction of 1.67 % by Wurz et al. (2010).

Species	O	Na	Mg	Al	Si	P	S
Abundance (%)	59.42	1.32	15.8	2.62	17.3	0.268	0.591
Species	K	Ca	Ti	Cr	Fe	Ni	Zn
Abundance (%)	0.030	1.670	0.014	0.041	0.611	0.004	0.285

the observations. For some elements like Ti and Cr, only upper limits are quoted from the measurements, which are compatible with the predictions by the model. For Na, Al, S and Ca the model predicts somewhat lower values, for Mg slightly higher values than observed. As discussed in Section 3.1, these differences have only a little effect on the resulting exosphere densities. Moreover, it should be noted that the reported measurements are not global averages, but for restricted areas on the surface, and show some local variation. For example, Peplowski et al. (2012) find that the average K abundance is 1150 and 1280 ppm for the areas sampled in 2011 and 2012, respectively. However, for individual locations the range of K abundances is between 754 and 1786 ppm. Similarly, Weider et al. (2012) find a range of abundances for many elements varying over a decade, depending on location on the surface. Considering the scatter between different measurements and the limited surface coverage, the agreement between the global abundances from Wurz et al. (2010) and the measurements is satisfactory (cf. Fig. 2).

In the present study we used the elemental surface composition derived from the multiplicative model with a fixed Calcium fraction of 1.67% from Wurz et al. (2010). The fractions are summarized in Table 2. A slightly modified composition model is briefly addressed in Section 3.1.

### 2.3. Sputter yields

The sputter yields were obtained by means of the 2013 version of the SRIM package (Ziegler et al., 1984, 2013; Ziegler, 2004). The calculations were performed for the multiplicative surface composition model with a fixed Ca fraction of 1.67 % (Table 2) with a surface mass density of  $3.11 \text{ g cm}^{-3}$  (Wurz et al., 2010) and an incident angle of impacting solar wind ions of  $45^\circ$  (Wurz et al., 2007). The sputter yields were calculated for the main constituents of impacting solar wind ions, i.e., for  $\text{H}^+$  and  $\text{He}^{++}$  ions. The contributions of heavier solar wind ions to the flux of sputtered material are less than 1% (Wurz et al., 2010) because these ion fluxes are very low (Wurz, 2005), thus they were neglected. The total sputter yield  $Y_i$  of species  $i$  was calculated by  $Y_i = x^{\text{H}} Y_i^{\text{H}} + x^{\text{He}} Y_i^{\text{He}}$ , where  $x^{\text{H}}$  and  $x^{\text{He}}$  are the fractions of  $\text{H}^+$  and  $\text{He}^{++}$  ions in the solar wind, respectively, and  $Y_i^{\text{H}}$  and  $Y_i^{\text{He}}$  are the sputter yields of species  $i$  caused by  $\text{H}^+$  and  $\text{He}^{++}$  ions respectively.

Fig. 3 illustrates the total oxygen sputter yields for various solar wind helium fractions in the range of the solar wind impact velocity from 100 to  $4000 \text{ km s}^{-1}$ . Helium sputtering is about 8 times more effective than proton-sputtering, thus for a typical solar wind helium fraction of 5%, about 30% of the total sputter yield is caused by helium sputtering. This fraction increases to 40% for a solar wind helium fraction of 8% and to 70% for a solar wind He fraction of 20%. The maximum sputter yield caused by  $\text{He}^{++}$  ions is about 0.53 oxygen atoms per impacting helium ion at an impact velocity of about  $200 \text{ km s}^{-1}$ , whereas protons produce at most 0.065 sputtered oxygen atoms per impacting proton at an impact velocity of about  $320 \text{ km s}^{-1}$ . For lower impact velocities

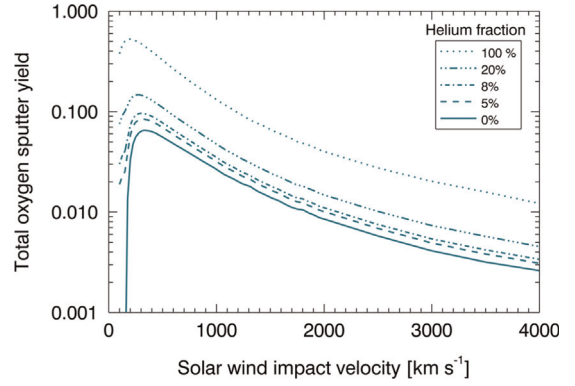


Fig. 3. Total oxygen sputter yields for different solar wind helium fractions.

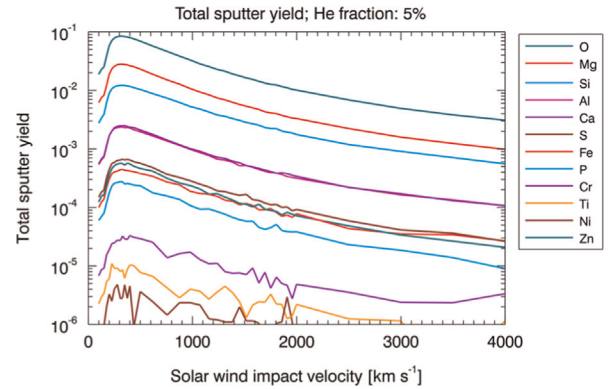


Fig. 4. Total sputter yields for 12 surface elements obtained by the multiplicative surface composition model with a fixed Ca fraction of 1.67% (Wurz et al., 2010). Sputter yields for Na and K are not shown since their contribution to the exosphere density is not considered in this paper.

the sputter yields decrease rather strong, especially in the case of helium sputtering.

Fig. 4 gives an overview of the total sputter yields of 12 species (without K and Na) according to the multiplicative surface model with fixed Ca fraction of 1.67% (Wurz et al., 2010). The total sputter yields cover a range of more than 4 magnitudes, resulting from the range of elemental abundances. Within a limited abundance range there is a linear relation between the total sputter yields and the elemental atomic surface fraction:  $Y_i = Y_i^{\text{el}} C_i$  (Wurz et al., 2007), which can be used for surface compositions very similar to the composition assumed to obtain the total sputter yields.

Mercury's resulting sputter flux  $\Phi_i^{\text{SP}}$  of species  $i$  is obtained by

$$\Phi_i^{\text{SP}}(\vartheta, \varphi) = \Phi^{\text{SW}}(\vartheta, \varphi) Y_i (1 - por), \quad (1)$$

with  $\Phi^{\text{SW}}(\vartheta, \varphi)$  being the solar wind flux ( $\text{H}^+$  and  $\text{He}^{++}$  ions) depending on latitude  $\vartheta$  and longitude  $\varphi$  as illustrated in Fig. 1,  $Y_i$  the total sputter yield of species  $i$  for the surface composition given in Table 2, and  $por$  the porosity of the regolith surface which is assumed to be 0.3 (Cassidy and Johnson, 2005; Wurz et al., 2010) and effectively reduces the sputter yield with regard to that of solid grains by 30%.

### 2.4. 3D exosphere modeling

The sputter yields of 12 chemical elements (see Table 2, without K and Na) caused by solar wind sputtering are the basic source in the modeling of Mercury's exosphere, which depends on latitude and longitude as described by the solar wind flux maps (see Fig. 1).

The production rate  $Q$  in units of  $s^{-1}$  of particles generated in a surface element is calculated by

$$Q = \int \phi_i^{sp} dA, \quad (2)$$

where  $A$  is the area and  $\phi_i^{sp}(\vartheta, \varphi)$  the corresponding sputter flux of the surface element, given by Eq. (1). We generate a total of about  $4 \times 10^6$  pseudo-particles equally distributed over Mercury's surface. With  $N$  being the number of pseudo-particles of the considered surface element the production rate  $Q_p$ , assigned to each pseudo-particle, is given by

$$Q_p = \frac{Q}{N}. \quad (3)$$

The energy distribution of the sputtered species is taken from Sigmund (1969) that was extended to account for the maximum energy which can be imparted to a sputtered particle (Wurz and Lammer, 2003; Wurz et al., 2007):

$$f(E_e) = \frac{6E_b}{3 - 8\sqrt{E_b/E_c}} \frac{E_e}{(E_e + E_b)^3} \left( 1 - \sqrt{\frac{E_e + E_b}{E_c}} \right) \quad (4)$$

with

$$E_c = E_i \frac{4m_1 m_2}{(m_1 + m_2)^2}, \quad (5)$$

where  $E_e$  and  $E_b$  are the kinetic energy and the surface binding energy of the sputtered particle with mass  $m_2$ , respectively, and  $E_i$  is the energy of the impacting particle  $m_1$ .

The binding energies used in the calculation are listed in Table 3 and are taken from the SRIM model.

The distribution of the angle  $\theta$  between the surface normal and the initial trajectory of the sputtered particle is assumed to follow the Knudsen cosine law (Cassidy and Johnson, 2005):

$$f(\beta) \propto \cos\theta. \quad (6)$$

In the horizontal plane the velocity vector is assumed to be distributed uniformly. Thus, we know the initial position and velocity vectors and the production rates of all pseudo-particles.

We divide the spherical space from Mercury's surface up to an altitude of 50 000 km into volume cells with a vertical resolution of 200 km, significantly less than the typical scale heights for sputtered species ( $h_O = 1600$  km,  $h_{Mg} = 1300$  km, and  $h_{Ca} = 890$  km, Wurz et al., 2010), and  $6^\circ$  in latitude and longitude, respectively. The trajectories of the pseudo-particles are calculated by means of a second order Runge–Kutta integration routine and the time  $t$  that the pseudo-particle needs to transverse each cell is determined. The contribution of this pseudo-particle to the number of particles  $N_{part}$  inside the cells is then given by  $N_{part} = Q_p t$ , and finally the number density  $n$  in the considered cell is obtained by summing up the contributions from all pseudo-particles and relating it to the cell volume  $V_c$ :

$$n = \frac{\sum N_{part}}{V_c}. \quad (7)$$

The integration of the particle trajectories is performed up to a distance of 50 000 km which is well within Mercury's sphere of influence so that the gravitational perturbation of the Sun can be neglected. The integration is terminated either when the particle exceeds this distance or when it falls back onto the surface, where we assume perfect sticking. We note that at 50 000 km altitude more than 99% of the particles have velocities exceeding the escape velocity, which justifies these particles to be treated as lost.

Depending on Mercury's radial velocity with respect to the Sun, which is a function of its orbital position, the effect of solar radiation acceleration cannot be neglected for the elements Sodium, Potassium and Calcium (Smyth and Marconi, 1995; Potter et al., 2007; Potter and Killen, 2008; McClintock et al., 2009). Also Magnesium experiences this effect, but it is a factor of  $4.7 \times 10^{-3}$  weaker than Mercury's surface gravity (McClintock et al., 2009) and will be neglected in this paper. Resonance scattering of solar radiation causes an acceleration  $a$  of the considered species

$$a = \frac{\pi h e^2 \nu}{m_e m c^2} \pi F_\nu \frac{f}{R^2}; \quad (8)$$

here,  $m$  is the mass of the species,  $e$  and  $m_e$  denote charge and mass of an electron,  $h$  is the Planck constant,  $\nu$  is the frequency and  $f$  is the oscillator strength of the resonance transition,  $\pi F_\nu$  is the solar flux for a specific frequency at 1 AU in the rest frame of the species and  $R$  the heliocentric distance in AU.

Photoionization rates are taken from Huebner et al. (1992), and the online tool available at <http://phidrates.space.swri.edu/> for both, the quiet and the active Sun and are listed in Table 3. The loss due to photoionization is taken into account by continuously reducing the production rate  $Q_p$ , assigned to the considered pseudo-particle, along its trajectory by the appropriate factor.

### 3. Results

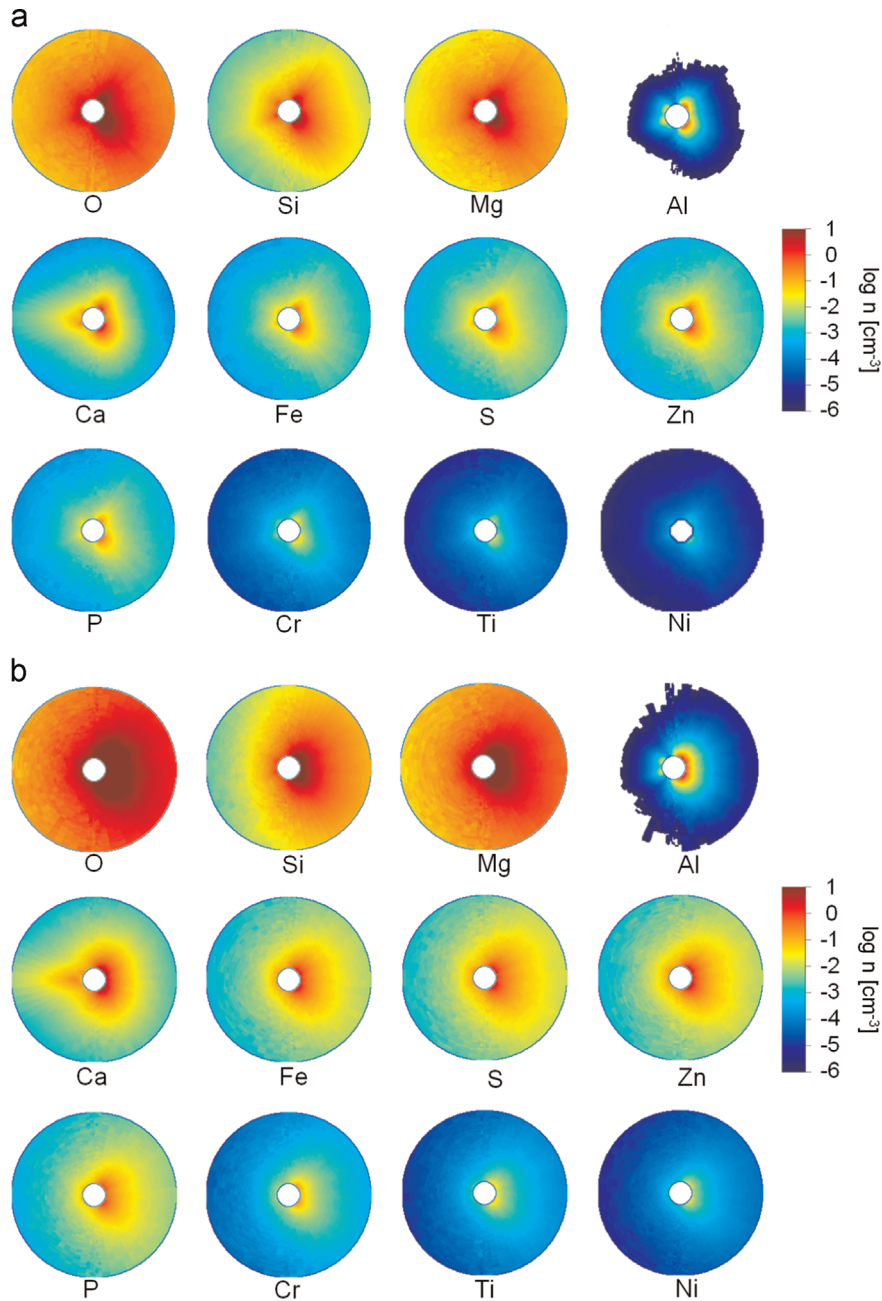
We compare the results for the typical case 1 and for the extreme event case 4 of all sputtered elements. Mercury's heliocentric distance was chosen in accordance with MESSENGER's first flyby (M1) at 0.35 AU corresponding to a true anomaly angle (TAA) of  $285^\circ$  (Vervack et al., 2010).

Fig. 5a illustrates the modeled number density in the noon–midnight plane (the Sun is to the right) for various refractory elements. Because of its high surface abundance (see Table 2), the oxygen density in the exosphere is significantly larger than the density of the other elements considered in this study. Although the model surface abundances of magnesium and silicon are similar, the magnesium density is enhanced with respect to silicon because it can be released easier due to its lower surface binding energy of 1.54 eV compared to the Si binding energy of 4.7 eV. The density of aluminium rapidly falls off with increasing distance from the planet because its photoionization rate is much larger than that of the other elements (Table 3). Among the elements considered, solar radiation acceleration is only relevant for Ca, yielding to a Ca tail in the anti-sunward direction. It should be noted that the maximum density values obtained for the elements are somewhat higher than those given by Wurz et al. (2010) because the precipitation rates of solar wind ions is not uniform over the surface. Higher ion precipitation fluxes at localized regions can lead to higher exospheric densities at the surface than the average densities published by Wurz et al. (2010). Fig. 5b displays the 3-dimensional exosphere density for the extreme case 4. With respect to case 1, the densities are significantly increased because

**Table 3**

Surface binding energies  $E_b$  in eV (according to the SRIM model) and photo ionization rates (PI) in  $10^{-6} s^{-1}$  for a solar distance of 1 AU (taken from Huebner et al., 1992) for the 14 species of the surface composition model.

Species	O	Na	Mg	Al	Si	P	S
$E_b$	2.0	2.0	1.54	3.36	4.70	3.27	2.88
PI (quiet Sun)	0.7	–	0.7	1200	23.2	0.6	1.1
PI (active Sun)	1.8	–	1.1	1300	48.5	1.4	2.3
Species	K	Ca	Ti	Cr	Fe	Ni	Zn
$E_b$	0.93	2.10	4.89	4.12	4.34	3.92	1.35
PI (quiet Sun)	–	69.6	2.5	3.8	1.8	0.9	0.5
PI (active Sun)	–	78.0	5.7	8.9	3.7	1.9	1.4



**Fig. 5.** Meridian volume density plots with the Sun at the right side for (a) case 1 and (b) case 4 within 6 Hermean radii (0–15 000 km altitude) around the planet. Note that both figures display the same color scaling. (For interpretation of the references to color in this figure caption, the reader is referred to the web version of this paper.)

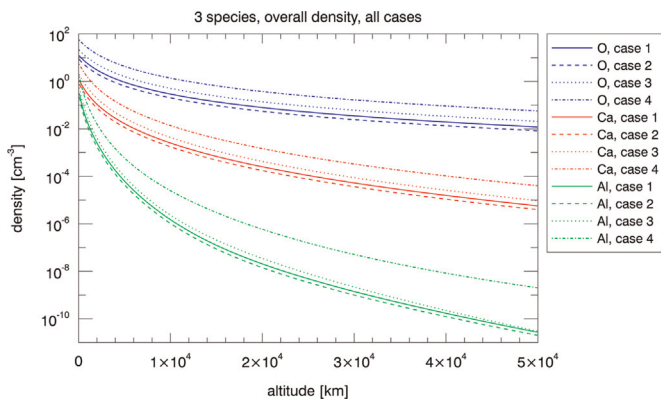


**Fig. 6.** Altitude density profiles of 3 selected species for all cases.

the solar wind can effectively sputter particles from the whole dayside surface of Mercury (compare Fig. 1).

Fig. 6 shows altitude density profiles averaged over the entire planet of 3 selected species for all 4 cases to compare the differences between them. For all elements case 2 results in lower densities compared to case 1, whereas case 3 shows slightly enhanced densities. Case 4 results in density enhancements of one to two orders of magnitude depending on the considered element and the altitude, although the corresponding sputter yields are about three times less than for case 1 (compare with Figs. 3 and 4); this is due to the enhanced solar wind flux in case 4.

In Fig. 7 altitude density profiles averaged over the entire planet are shown for the cases 1 and 4 for all considered species. Al and Ca have lower scale heights than the other elements because of the high photoionization rate for Al and the radiation acceleration effect of Ca which reduces the scale height. Fig. 8 displays

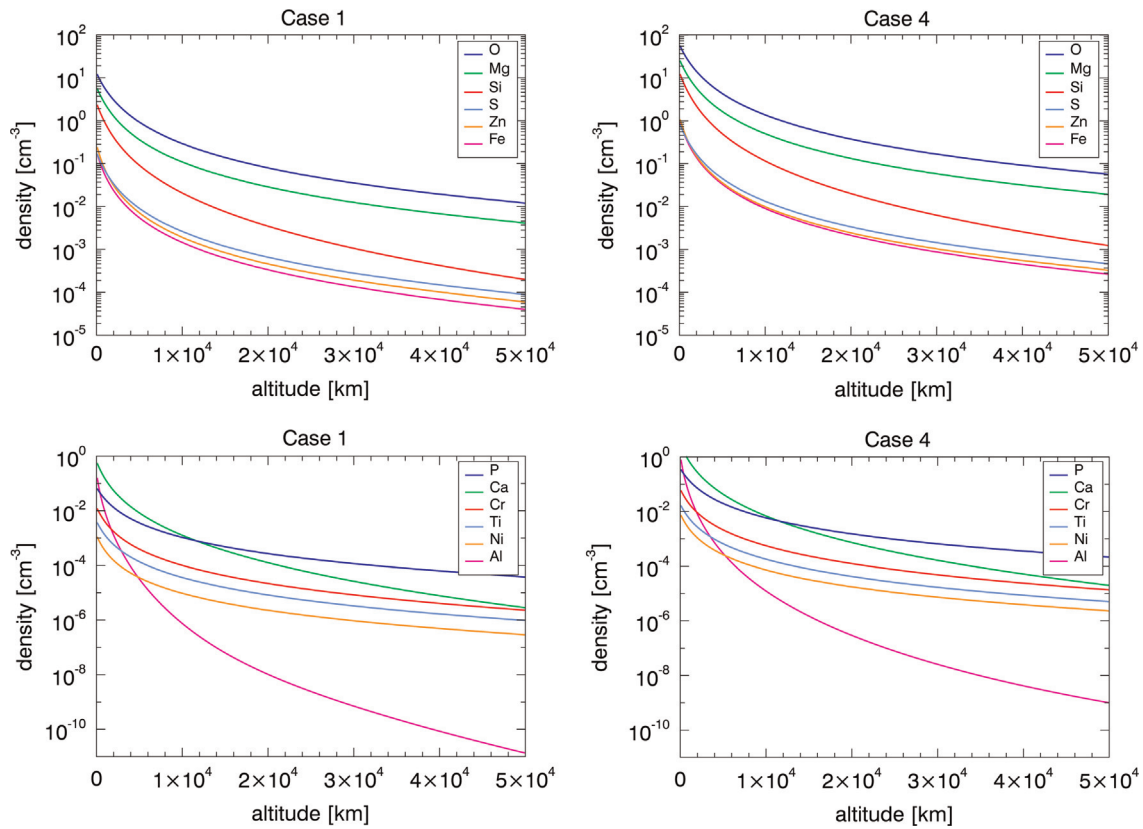


Fig. 7. Altitude density profiles of all considered species for case 1 (left panels) and case 4 (right panels).

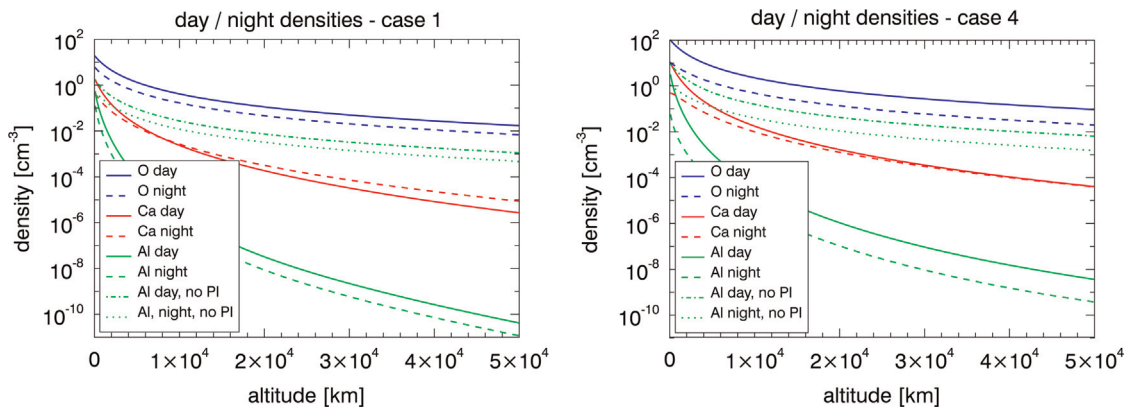


Fig. 8. Day/nightside profiles for case 1 (left panel) and case 4 (right panel). For Al both profiles with and without photoionization (PI) are shown.

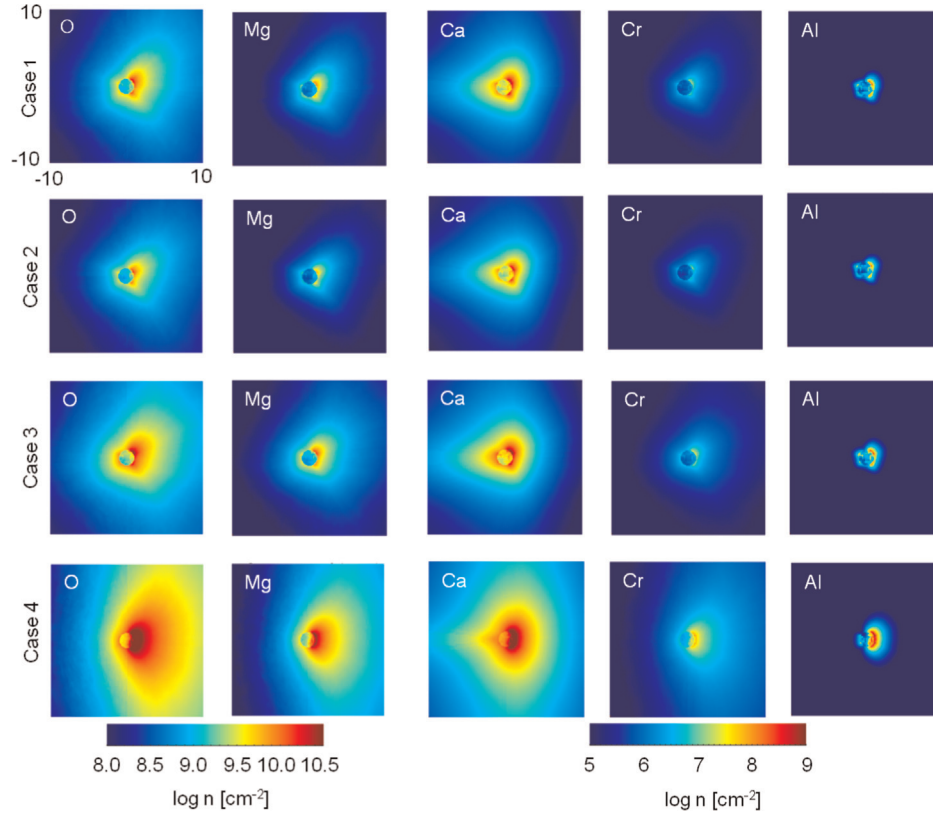
the density profiles of three species for the cases 1 (left panel) and 4 (right panel) obtained by averaging the density separately over the day- and nightside. Nightside densities are always lower than the density at dayside with the exception of Ca, where the particles are transported into the nightside hemisphere due to the solar radiation acceleration. For case 1, at about 8000 km altitude, the nightside Ca-density exceeds the dayside Ca-density, while for case 4, the nightside density starts to exceed the dayside density at 50 000 km height. Fig. 8 also includes the density profile of aluminium when photoionization is neglected (annotated by 'no PI'), showing that Al is diminished at higher altitudes due to photoionization by several orders of magnitude.

Fig. 9 illustrates column densities of selected elements obtained by moving along a line parallel to the Sun–planet line at 10 planetary radii and looking towards the noon–midnight plane of the planet. The density integrated along these lines of sight is projected onto the noon–midnight plane and displayed in Fig. 9. The

four rows correspond to the cases 1–4. Note the different scaling of O and Mg with respect to the other elements. While the column densities are quite similar for cases 1 and 2, the calculated column densities increase with increased IMF and solar wind density (case 3) and become significantly larger for the high solar wind bulk velocity (case 4).

In the latter case, the entire dayside surface of the planet experiences intense ion sputtering which results in column densities enhanced by more than one order of magnitude with respect to the nominal conditions of case 1. Due to the effective photoionization, even in the extreme case 4 higher Al densities are expected only in a relatively small volume above the dayside of Mercury, while the nightside remains almost unaffected by the stronger solar wind.

Table 4 lists numerical values of column densities in units of  $10^8 \text{ cm}^{-2}$  obtained at various local times of Mercury when viewed from a distance of 10 planetary radii in the equatorial plane. Fig. 10



**Fig. 9.** Column densities for the cases 1–4 obtained by passing the planet along a line parallel to the Sun–planet direction at 10 planetary radii and projecting the density integrated along the lines of sight onto the noon–midnight plane of Mercury. Each image displays a region of  $20 \times 20$  Hermean radii.

**Table 4**

Column densities as seen from four different positions on a circle of 10 planetary radii in the equatorial plane when viewed to three different locations (with latitude  $\varphi = 0^\circ, \pm 45^\circ$ ) on Mercury's surface. Longitude ( $lon = 0^\circ, \pm 90^\circ, 180^\circ$ ) correspond to subsolar point, terminator and midnight, respectively, (see Fig. 10).

Column density ( $\text{cm}^{-2}$ ) $\times 10^8$																
lon	–180	–90	0	90	–180	–90	0	90	–180	–90	0	90	–180	–90	0	90
<b>O</b>	<b>case 1</b>				<b>case 2</b>				<b>case 3</b>				<b>case 4</b>			
$\varphi = 45^\circ$	9.65	11.1	71.4	12.8	7.51	9.40	53.3	10.7	15.9	27.1	120.3	38.3	19.5	73.3	283.7	39.9
$0^\circ$	7.78	13.5	29.8	17.5	5.84	9.50	20.4	17.8	11.9	22.1	58.2	35.1	17.4	81.1	193.9	33.6
$-45^\circ$	9.37	12.3	33.8	40.1	6.78	10.6	22.7	25.5	3.8	15.6	47.7	80.2	20.8	95.5	227.5	46.1
<b>Mg</b>	<b>case 1</b>				<b>case 2</b>				<b>case 3</b>				<b>case 4</b>			
$\varphi = 45^\circ$	4.2	4.9	29.7	5.4	3.2	4.1	21.9	4.5	6.9	11.9	50.0	12.3	9.0	29.0	114.5	17.8
$0^\circ$	3.4	5.7	12.2	7.5	2.6	4.1	8.4	7.5	5.3	9.2	20.1	14.7	7.5	33.3	77.9	14.2
$-45^\circ$	4.1	5.3	14.3	17.1	3.0	4.5	9.7	10.7	5.9	6.8	20.0	34.1	9.7	39.0	94.1	20.1
<b>Ca</b>	<b>case 1</b>				<b>case 2</b>				<b>case 3</b>				<b>case 4</b>			
$\varphi = 45^\circ$	0.3	0.2	1.7	0.2	0.2	0.2	1.3	0.2	0.5	0.5	2.8	0.5	0.6	1.7	6.3	0.8
$0^\circ$	0.4	0.3	0.4	0.3	0.3	0.2	0.3	0.4	0.6	0.4	0.7	0.6	0.9	2.1	3.5	0.6
$-45^\circ$	0.3	0.2	0.7	0.9	0.2	0.2	0.4	0.6	0.4	0.3	0.8	1.9	0.7	2.6	5.0	1.1
<b>Cr</b>	<b>case 1</b>				<b>case 2</b>				<b>case 3</b>				<b>case 4</b>			
$\varphi = 45^\circ$	0.01	0.01	0.05	0.01	<0.01	0.01	0.03	0.01	0.01	0.01	0.07	0.01	0.01	0.05	0.19	0.03
$0^\circ$	<0.01	0.01	0.02	0.01	<0.01	0.01	0.01	0.01	0.01	0.01	0.03	0.02	0.01	0.05	0.13	0.02
$-45^\circ$	0.01	0.01	0.02	0.03	<0.01	0.01	0.01	0.02	0.01	0.01	0.03	0.05	0.01	0.06	0.16	0.03
<b>Al</b>	<b>case 1</b>				<b>case 2</b>				<b>case 3</b>				<b>case 4</b>			
$\varphi = 45^\circ$	0.01	<0.01	0.21	<0.01	0.01	0.01	0.16	<0.01	0.02	0.04	0.34	0.01	<0.01	0.04	0.80	0.04
$0^\circ$	0.01	0.03	0.03	0.02	0.01	0.01	0.02	0.04	0.01	0.03	0.04	0.02	<0.01	0.07	0.39	0.02
$-45^\circ$	0.01	0.02	0.09	0.09	0.01	0.02	0.06	0.05	0.01	0.01	0.08	0.15	0.01	0.09	0.59	0.06

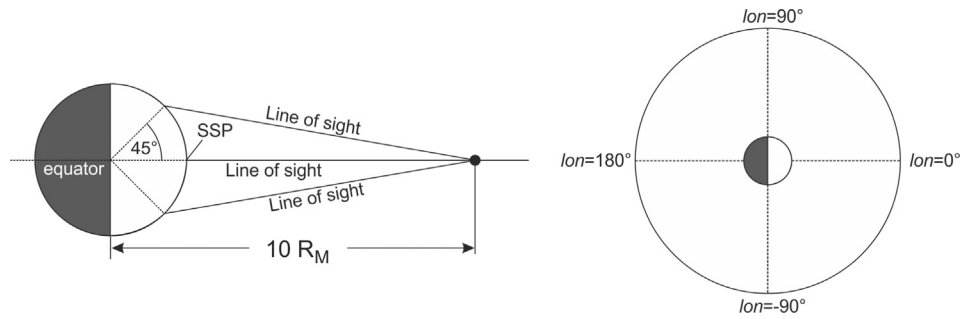


**Fig. 10.** Left: Line of sight from a distance of 10 Mercury radii to three different locations on Mercury [(0,0)=subsolar point (SSP), (0, - 45°), (0, 45°)] along the zero longitude on Mercury. Right: The four vantage points for which column densities are listed in Table 4.

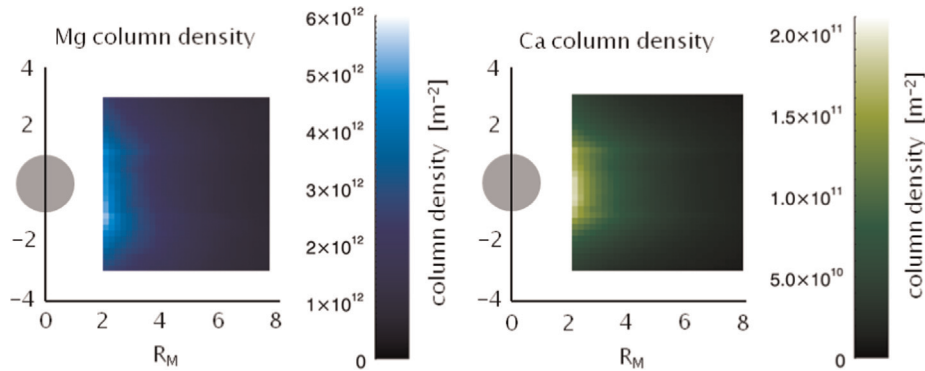


**Fig. 11.** Simulated column densities of Mg and Ca for case 1 projected onto the plane defined by Mercury's north pole and the Sun–Mercury line. (For interpretation of the references to color in this figure caption, the reader is referred to the web version of this paper.)

**Table 5**  
Impact and escape rates of various refractory elements.

Species	Case 1		Case 2		Case 3		Case 4	
	Impact (s <sup>-1</sup> )	Escape (s <sup>-1</sup> )	Impact (s <sup>-1</sup> )	Escape (s <sup>-1</sup> )	Impact (s <sup>-1</sup> )	Escape (s <sup>-1</sup> )	Impact (s <sup>-1</sup> )	Escape (s <sup>-1</sup> )
O	4.9·10 <sup>23</sup>	2.0·10 <sup>24</sup>	3.4·10 <sup>23</sup>	1.4·10 <sup>24</sup>	8.6·10 <sup>23</sup>	3.4·10 <sup>24</sup>	2.2·10 <sup>24</sup>	1.0·10 <sup>25</sup>
Si	6.5·10 <sup>22</sup>	5.4·10 <sup>22</sup>	4.5·10 <sup>22</sup>	3.7·10 <sup>22</sup>	1.2·10 <sup>23</sup>	9.0·10 <sup>22</sup>	3.3·10 <sup>23</sup>	3.9·10 <sup>23</sup>
Mg	2.6·10 <sup>23</sup>	5.6·10 <sup>23</sup>	1.8·10 <sup>23</sup>	3.9·10 <sup>23</sup>	4.6·10 <sup>23</sup>	9.4·10 <sup>23</sup>	1.2·10 <sup>24</sup>	2.9·10 <sup>24</sup>
Al	6.7·10 <sup>19</sup>	3.5·10 <sup>16</sup>	4.7·10 <sup>19</sup>	2.6·10 <sup>16</sup>	1.2·10 <sup>20</sup>	3.4·10 <sup>16</sup>	3.1·10 <sup>20</sup>	4.4·10 <sup>18</sup>
Ca	1.1·10 <sup>22</sup>	1.2·10 <sup>21</sup>	7.6·10 <sup>21</sup>	8.7·10 <sup>20</sup>	1.9·10 <sup>22</sup>	2.1·10 <sup>21</sup>	5.7·10 <sup>22</sup>	1.0·10 <sup>22</sup>
Fe	8.0·10 <sup>21</sup>	4.2·10 <sup>21</sup>	5.6·10 <sup>21</sup>	2.9·10 <sup>21</sup>	1.4·10 <sup>22</sup>	6.8·10 <sup>21</sup>	4.4·10 <sup>22</sup>	3.3·10 <sup>22</sup>
S	8.1·10 <sup>21</sup>	1.1·10 <sup>22</sup>	5.6·10 <sup>21</sup>	7.7·10 <sup>21</sup>	1.4·10 <sup>22</sup>	1.8·10 <sup>22</sup>	3.8·10 <sup>22</sup>	6.5·10 <sup>22</sup>
Zn	1.2·10 <sup>22</sup>	5.0·10 <sup>21</sup>	8.4·10 <sup>21</sup>	3.5·10 <sup>21</sup>	2.0·10 <sup>22</sup>	7.5·10 <sup>21</sup>	5.4·10 <sup>22</sup>	3.5·10 <sup>22</sup>
P	3.2·10 <sup>21</sup>	4.6·10 <sup>21</sup>	2.2·10 <sup>21</sup>	3.2·10 <sup>21</sup>	5.5·10 <sup>21</sup>	7.6·10 <sup>21</sup>	1.6·10 <sup>22</sup>	2.9·10 <sup>22</sup>
Cr	5.5·10 <sup>20</sup>	2.9·10 <sup>20</sup>	3.8·10 <sup>20</sup>	2.0·10 <sup>20</sup>	8.6·10 <sup>20</sup>	4.2·10 <sup>20</sup>	2.7·10 <sup>21</sup>	2.0·10 <sup>21</sup>
Ti	1.7·10 <sup>20</sup>	1.1·10 <sup>20</sup>	1.2·10 <sup>20</sup>	7.9·10 <sup>19</sup>	1.9·10 <sup>20</sup>	1.3·10 <sup>20</sup>	7.7·10 <sup>20</sup>	7.1·10 <sup>20</sup>
Ni	5.4·10 <sup>19</sup>	2.7·10 <sup>19</sup>	3.8·10 <sup>19</sup>	1.9·10 <sup>19</sup>	1.6·10 <sup>20</sup>	6.9·10 <sup>19</sup>	3.6·10 <sup>20</sup>	2.6·10 <sup>20</sup>

(left) illustrates how the column densities in Table 4 are obtained at a longitude of  $lon = 0^\circ$  for three different latitudes of  $-45^\circ$ ,  $0^\circ$  and  $45^\circ$ . In a similar way, the column densities at dusk ( $lon=90^\circ$ ), midnight ( $lon=180^\circ$ ), and dawn ( $lon=-90^\circ$ ) are obtained.

Although the magnetic field configuration was different for M1 and M2, the orbital parameters of Mercury and the radiation acceleration were quite similar (Vervack et al., 2010), suggesting comparable column densities during M1 and M2. Fig. 11 displays the simulated column densities of Mg and Ca for case 1 (corresponding to M1 conditions) in the nightside of Mercury by using a linear color scale to allow a better comparison with MESSENGER tail observations, where radiance maps of Mg and Ca were recorded as the spacecraft approached the planet (McClintock et al., 2009). Reported column emissions for Mg and Ca cover a range of up to 250 and 600 Rayleighs, respectively, during the second flyby.

Using the published  $g$ -values of  $g=0.318$  for Mg and  $g=22.07$  for Ca (Vervack et al., 2010), this corresponds to a column density range of approximately up to  $8 \cdot 10^{12}$  and  $3 \cdot 10^{11} \text{ m}^{-2}$ , respectively, and is in reasonable agreement with the simulation results displayed in Fig. 11.

The MESSENGER spacecraft measured Ca emissions with its surface composition spectrometer since March 2011 on nearly a daily basis (Burger et al., 2014). That is, the dayside Ca exosphere was observed over more than 8 Mercury years. Prior to MESSENGER's orbit insertion, Burger et al. (2012) concluded from the initial observations that the detected Ca is most likely supplied by an energetic source that can be characterized by a temperature of more than 20 000 K and which is centered on or near the equatorial dawn, if one assumes a Maxwellian distribution.

Furthermore, these authors suggested that the observed Ca distribution did not appear to be related to either magnetospheric effects or material that had built up on the nightside so that it could have been desorbed as it rotated into the sunlight.

The recent results on the source rates and their seasonal variations presented in Burger et al. (2014) are more or less consistent with the previous analysis and conclusions of Burger et al. (2012). The long term data suggest a temperature of up to 50 000 K for the Ca source, although the previous assumed that 20 000 K also work well. The temperature differences appear because in Burger et al. (2012) the data have mainly been analyzed over Mercury's nightside, while in Burger et al. (2014) only dayside data have been used, where Ca was assumed to be symmetrically distributed over the day- and nightside. In reality, however, there may be an asymmetry of the source across the terminator.

From the observational results of Mercury's Ca exosphere component one can conclude that there should be an approximately constant source which is located in the dawn of the equatorial region with a constant size and energy. This source releases Ca with velocities higher than the escape velocity and with rates between  $\sim 4 \times 10^{22}$  and  $3.7 \times 10^{23} \text{ s}^{-1}$  at  $195^\circ$  and  $20^\circ$  true anomaly, respectively (Burger et al., 2014). Moreover, there seems to be no evidence of a year-to-year variability in the near surface dayside Ca exosphere; the peak Ca amount in the exosphere over one Mercury year varies from less than  $1 \text{ cm}^{-3}$  to  $\sim 4 \text{ cm}^{-3}$  (Burger et al., 2014).

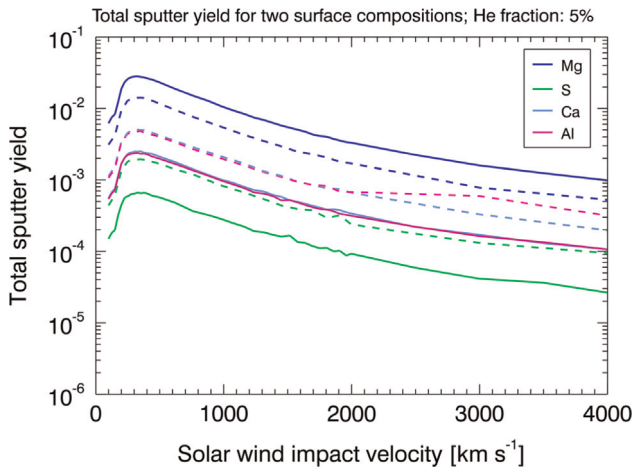


**Fig. 12.** Total sputter yields for the modified surface composition model (solid lines) for Mg, S, Ca, and Al. The dashed lines show the corresponding sputter yields of the unmodified model.

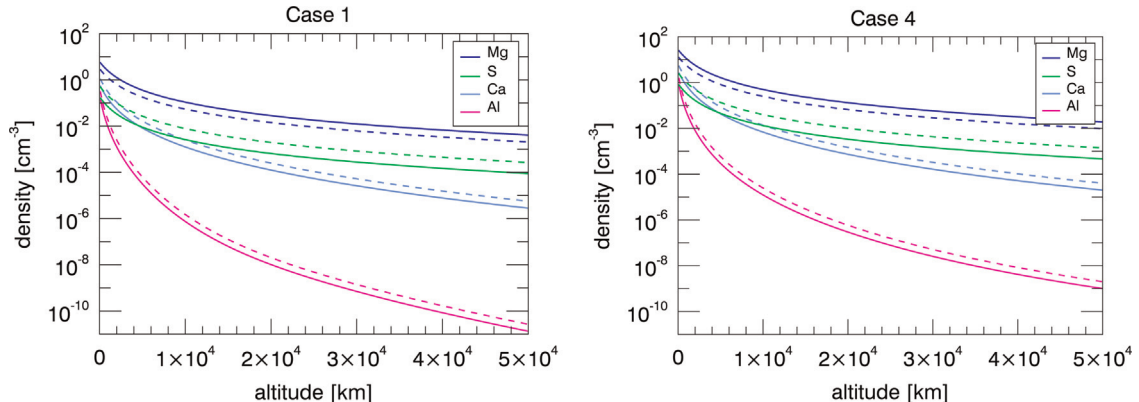


**Fig. 13.** Altitude density profiles of Mg, S, Ca, and Al resulting from the modified model for case 1 (left panel) and case 4 (right panel). Dashed lines correspond to the profiles of the original model.

As one can see from Fig. 1a–c – besides high energetic solar events (Fig. 1d) – solar wind induced ion precipitation can be associated with regions around high latitudes focused at the cusp areas. According to Fig. 8 (left panel), the modeled average dayside number density caused by solar wind sputtering is less than  $1 \text{ cm}^{-3}$  and is thus only a minor population with respect to the observations reported by Burger et al. (2014). A dayside Ca surface density comparable to the long-term observations is only expected due to sputtering during extreme solar events when the proton flux precipitates over the whole dayside (Fig. 8 right panel).

Because the dayside Ca exosphere density remains stable during nominal solar wind conditions and Burger et al. (2014) found no high-latitude Ca emission sources, these authors consider impact vaporization of micrometeorites as a promising scenario for explaining the observed Ca source (Cintala, 1992; Berzhnoy and Klumov, 2008; Borin et al., 2009; Berzhnoy, 2013; Grotheer and Livi, 2005; Killen and Hahn, 2015). In such a case impacts produce Ca mainly in molecular form in the impact plumes, where these molecules are quickly photodissociated and release energetic Ca atoms (Killen et al., 2005; Berzhnoy and Klumov, 2008; Berzhnoy, 2013). Our simulations of solar wind sputtered Ca also suggest that sputtering cannot explain the MESSENGER observations analyzed by Burger et al. (2014), although a less dense sputtered Ca population might be hidden in the observations. The major contribution to the Ca density should come from other processes like, e.g., impact vaporization of micrometeoroids. It should be noted that these conclusions also hold for the modified composition model, where the relative Ca fraction is increased (see Section 3.1).

The impact rates of sputtered particles falling back on the surface of Mercury and the escape rates of exospheric particles are listed in Table 5 for the four cases considered. For oxygen, the escape rates distinctly exceed the impact rates, because the sputter distribution, Eq. (4), peaks close to the escape energy so that a considerable amount of sputtered oxygen atoms will acquire velocities above the escape velocity. For the other species, however, the distribution function peaks at lower energies than the escape energy, leading to an increased generation of particles along bound orbits, which eventually fall back onto the surface. Over a long period, the large variation of the escape rates of different species may result in a distinct fractionation of the surface composition, in particular suggesting a strong depletion of the oxygen content of the surface.

### 3.1. Modified composition model

Given the error bars shown in Fig. 2, the modeled weight percent of Na, Mg, Al, and S are somewhat lower than those observed. To better agree with these measurements, we have

increased the weight percent of Na, Al, and Ca by a factor of 2 and that of S by a factor of 3. In addition, the weight percent of Mg has been divided by two. After having adjusted the compositional model accordingly, the total sputter yields for the modified surface composition have been recalculated and are displayed in Fig. 12 (solid lines) for Ca, Mg, Al, and S together with the corresponding yields of the original model (dashed lines). The figure indicates that the yields respond approximately linear to the change in the composition.

Fig. 13 shows the altitude density profiles of the four elements whose weight percent fraction has been modified. As expected, the density closely scales with the surface fraction of the elements, resulting in an increased density by a factor of two (Al and Ca) and three (S) and in half of the density for Mg.

#### 4. Summary and conclusion

A 3D hybrid solar wind interaction model has been applied to a global mineralogical surface composition model of Mercury. The resulting sputtered refractory elements and their release into the planet's exosphere, the corresponding density distributions from the surface up to 50 000 km and the escape rates have been simulated for various solar wind conditions. It is shown that the exosphere density of O, Mg, Al, Si, P, S, Ca, Ti, Cr, Fe, Ni, and Zn, compared to quiet or moderate solar wind conditions, can be enhanced by more than one order of magnitude during fast and denser solar wind events, where Mercury's magnetosphere is so compressed by the plasma ram pressure that  $H^+$  and  $He^{++}$  ions can precipitate onto the planet's surface over the whole dayside. Our results are also in agreement with MESSENGER observations of exospheric Ca and Mg particles. Less abundant refractory elements, which are difficult to observe during nominal solar wind conditions, may become temporarily detectable when the planet is hit by a fast and dense plasma cloud.

#### References

- Anderson, B.J., Johnson, C.L., Korth, H., Purucker, M.E., Winslow, R.M., Slavin, J.A., Solomon, S.C., McNutt Jr., R.L., Raines, J.M., Zurbuchen, T.H., 2011. The global magnetic field of Mercury from MESSENGER orbital observations. *Science* 333, 1859–1862.
- Baker, D.N., Odstrcil, D., Anderson, B.J., Arge, C.N., Benna, M., Gloeckler, G., Korth, H., Mayer, L.R., Raines, J.M., Schriver, D., Slavin, J.A., Solomon, S.C., Trávníček, P.M., Zurbuchen, T.H., 2011. The space environment of Mercury at the times of the second and third messenger flybys. *Planet. Space Sci.* 59, 2066–2074.
- Baker, D.N., Odstrcil, D., Anderson, B.J., Arge, C.N., Benna, M., Gloeckler, G., Raines, J.M., Schriver, D., Slavin, J.A., Solomon, S.C., Killen, R.M., Zurbuchen, T.H., 2009. Space environment of Mercury at the time of the first messenger flyby: solar wind and interplanetary magnetic field modeling of upstream conditions. *J. Geophys. Res.* 114.
- Berzhnoy, A.A., 2013. Chemistry of impact events on the moon. *Icarus*, 205–211.
- Berzhnoy, A.A., Klumov, B.A., 2008. Impacts as sources of the exosphere on mercury. *Icarus*, 511–522.
- Bida, T.A., Killen, R.M., Morgan, T.H., 2000. Discovery of calcium in Mercury's atmosphere. *Nature* 404, 159–161.
- Borin, P., Cremonese, G., Marzari, F., Bruno, M., Marchi, S., 2009. Statistical analysis of micrometeoroids flux on Mercury. *Astron. Astrophys.* 503, 259–264.
- Burger, M.H., Killen, R.M., McClintock, W.E., Merkel, A.W., Vervack Jr., R.J., Cassidy, T.A., Sarantos, M., 2014. Seasonal variations in Mercury's dayside calcium exosphere. *Icarus* 238, 51–58.
- Burger, M.H., Killen, R.M., McClintock, W.E., Vervack Jr., R.J., Merkel, A.W., Sprague, A.L., Sarantos, M., 2012. Modelling MESSENGER observations of calcium in Mercury's exosphere. *J. Geophys. Res.* 117, E00L11.
- Cassidy, T., Johnson, R., 2005. Monte Carlo model of sputtering and other ejection processes within a regolith. *Icarus* 176, 499–507.
- Cintala, M.J., 1992. Impact-induced thermal effects in the lunar and Mercurian regoliths. *J. Geophys. Res.* 131, 947–973.
- Evans, L.G., Peplowski, P.N., Rhodes, E.A., Lawrence, D.J., McCoy, T.J., Nittler, L.R., Solomon, S., Sprague, A.L., Stockstill-Cahill, K.R., Starr, R.D., Weider, S.Z., Boynton, W.V., Hamara, D.K., Goldsten, J.O., 2012. Major-element abundances on the surface of Mercury: Results from the MESSENGER gamma-ray spectrometer. *J. Geophys. Res.* 117, E00L07.
- Fjeldbo, G., Kliore, A., Sweetnam, D., Esposito, P., Seidel, B., Howard, T., 1976. The occultation of mariner 10 by mercury. *Icarus* 29, 407–415.
- Grotheer, E.B., Livi, S.A., 2005. Small meteoroids' major contribution to Mercury's exosphere. *Icarus* 173, 300–311.
- Hapke, B., 2001. Space weathering from Mercury to the asteroid belt. *J. Geophys. Res.* 106, 10039–10074.
- Huebner, W.F., Keady, J.J., Lyon, S.P., 1992. Solar photo rates for planetary atmospheres and atmospheric pollutants. *Astrophys. Space Sci.* 195, 1–294.
- Hunten, D., Morgan, T., Shemansky, D., 1988. Vilas, F., Chapman, C.R., Matthews, M. S. (Eds.), *The Mercury Atmosphere*. University of Arizona Press, Tucson, p. 562.
- Johnson, C.L., Purucker, M.E., Korth, H., Anderson, B.J., Winslow, R.M., Al Asad, M.M. H., Slavin, J.A., Alexeev, I.I., Phillips, R.J., Zuber, M.T., Solomon, S.C., 2012. MESSENGER observations of Mercury's magnetic field structure. *J. Geophys. Res.* 117.
- Kallio, E., Janhunen, P., 2003a. Modelling the solar wind interaction with Mercury by a quasi-neutral hybrid model. *Ann. Geophys.* 21, 2133–2145.
- Kallio, E., Janhunen, P., 2003b. Solar wind and magnetospheric ion impact on Mercury's surface. *Geophys. Res. Lett.* 30, 1877.
- Kallio, E., Janhunen, P., 2004. The response of the Hermean magnetosphere to the interplanetary magnetic field. *Adv. Space Res.* 33, 2176–2181.
- Killen, R., Cremonese, G., Lammer, H., Orsini, S., Potter, A.E., Sprague, A.L., Wurz, P., Khodachenko, M.L., Lichtenegger, H.I.M., Milillo, A., Mura, A., 2007. Processes that promote and deplete the exosphere of Mercury. *Space Sci. Rev.* 132, 433–509.
- Killen, R.M., Bida, T.A., Morgan, T.H., 2005. The calcium exosphere of Mercury. *Icarus* 173, 300–311.
- Killen, R.M., Hahn, J.M., 2015. Impact vaporization as a possible source of Mercury's calcium exosphere. *Icarus* 250, 230–237.
- McClintock, W.E., Izenberg, N.R., Holsclaw, G.M., Blewett, D.T., Domingue, D.L., Head, J.W., Helbert, J., McCoy, T.J., Murchie, S.L., Robinson, M.S., Solomon, S.C., Sprague, A.L., Vilas, F., 2008. Spectroscopic observations of Mercury's surface reflectance during MESSENGER's first Mercury flyby. *Science* 321, 62–65.
- McClintock, W.E., Vervack, R.J., Bradley, E.T., Killen, R.M., Mouawad, N., Sprague, A.L., Burger, M.H., Solomon, S.C., Izenberg, N.R., 2009. MESSENGER observations of Mercury's exosphere: Detection of magnesium and distribution of constituents. *Science* 324, 610.
- Nittler, L.R., Starr, R.D., Weider, S.Z., McCoy, T.J., Boynton, W.V., Ebel, D.S., Ernst, C.M., Evans, L.G., Goldsten, J.O., Hamara, D.K., Lawrence, D.J., McNutt, R.L., Schlemm, C.E., Solomon, S.C., Sprague, A.L., 2011. The major-element composition of Mercury's surface from MESSENGER X-ray spectrometry. *Science* 333, 1847–1850.
- Peplowski, P.N., Evans, L.G., Hauck, S.A., McCoy, T.J., Boynton, W.V., Gillis-Davis, J.J., Ebel, D.S., Goldsten, J.O., Hamara, D.K., Lawrence, D.J., McNutt, R.L., Nittler, L.R., Solomon, S.C., Rhodes, E.A., Sprague, A.L., Starr, R.D., Stockstill-Cahill, K.R., 2011. Radioactive elements on Mercury's surface from MESSENGER: Implications for the planets formation and evolution. *Science* 333, 1850–1852.
- Peplowski, P.N., Lawrence, D.J., Rhodes, E.A., Sprague, A.L., McCoy, T.J., Denevi, B.W., Evans, L.G., Head, J.W., Nittler, L.R., Solomon, S.C., Stockstill-Cahill, K.R., Weider, S.Z., 2012. Variations in the abundances of potassium and thorium on the surface of Mercury: results from the MESSENGER gamma-ray spectrometer. *J. Geophys. Res.: Planets* 117.
- Potter, A.E., Killen, R.M., 2008. Observations of the sodium tail of Mercury. *Icarus* 194, 1–12.
- Potter, A.E., Killen, R.M., Morgan, T.H., 2007. Solar radiation acceleration effects on Mercury sodium emission. *Icarus* 186, 571–580.
- Rhodes, E.A., Evans, L.G., Nittler, L.R., Starr, R.D., Sprague, A.L., Lawrence, D.J., McCoy, T.J., Stockstill-Cahill, K.R., Goldsten, J.O., Peplowski, P.N., Hamara, D.K., Boynton, W.V., Solomon, S.C., 2011. Analysis of MESSENGER Gamma-Ray Spectrometer data from the Mercury flybys. *Planet. Space Sci.* 59, 1829–1841.
- Sigmund, P., 1969. Theory of sputtering. I. Sputtering yield of amorphous and polycrystalline targets. *Phys. Rev.* 184, 383–416.
- Slavin, J.A., DiBraccio, G.A., Gershman, D.J., Imber, S.M., Poh, G.K., Raines, J.M., Zurbuchen, T.H., Jia, X., Baker, D.N., Glassmeier, K.H., Livi, S.A., Boardsen, S.A., Cassidy, T.A., Sarantos, M., Sundberg, T., Masters, A., Johnson, C.L., Winslow, R.M., Anderson, B.J., Korth, H., McNutt Jr., R.L., Solomon, S.C., 2014. MESSENGER observations of Mercury's dayside magnetosphere under extreme solar wind conditions. *J. Geophys. Res.* 119, 8087–8116.
- Slavin, J.A., Lepping, R.P., Wu, C.C., Anderson, B.J., Baker, D.N., Benna, M., Boardsen, S.A., Killen, R.M., Korth, H., Krimigis, S.M., et al., 2010. MESSENGER observations of large flux transfer events at Mercury. *Geophys. Res. Lett.* 37, L02105.
- Smyth, W.H., Marconi, M.L., 1995. Theoretical overview and modeling of the sodium and potassium atmospheres of Mercury. *Astrophys. J.* 441, 839–864.
- Sprague, A., Warell, J., Cremonese, G., Langevin, Y., Helbert, J., Wurz, P., Veselovsky, I., Orsini, S., Milillo, A., 2007. Mercury's surface composition and character as measured by ground-based observations. *Space Sci. Rev.* 132, 399–431.
- Sprague, A.L., Donaldson Hanna, K.L., Kozlovsky, R.W.H., Helbert, J., Maturilli, A., Warell, J.B., Hora, J.L., 2009. Spectral emissivity measurements of Mercury's surface indicate Mg- and Ca-rich mineralogy, K-spar, Na-rich plagioclase, rutile, with possible perovskite, and garnet. *Planet. Space Sci.* 57, 364–383.
- Starr, R.D., Schriver, D., Nittler, L.R., Weider, S.Z., Byrne, P.K., Ho, G.C., Rhodes, E.A., Schlemm, C.E., Solomon, S.C., Trávníček, P.M., 2012. MESSENGER detection of electron-induced X-ray fluorescence from Mercury's surface. *J. Geophys. Res.* 117, 1–19.
- Vervack, R.J., McClintock, W.E., Killen, R.M., Sprague, A.L., Anderson, B.J., Burger, M.H., Bradley, E.T., Mouawad, N., Solomon, S.C., Izenberg, N.R., 2010. Mercury's complex exosphere: Results from MESSENGER's third flyby. *Science* 329, 672.

- Warell, J., Sprague, A.L., Emery, J.P., Kozlowsky, R.W.H., Long, A., 2006. The 0.7–5.3  $\mu\text{m}$  IR spectra of Mercury and the Moon: Evidence for high-Ca clinopyroxene on Mercury. *Icarus* 180, 281–291.
- Weider, S.Z., Nittler, L.R., Starr, R.D., McCoy, T.J., Stockstill-Cahill, K.R., Byrne, P.K., Denevi, B.W., Head, J.W., Solomon, S.C., 2012. Chemical heterogeneity on Mercury's surface revealed by the MESSENGER X-Ray Spectrometer. *J. Geophys. Res.: Planets*, 117.
- Wurz, P., 2005. Solarwind composition. In: *The Dynamic Sun: Challenges for Theory and Observations*, ESA. pp. 1–9.
- Wurz, P., Lammer, H., 2003. Monte-Carlo simulation of Mercury's exosphere. *Icarus* 164, 1–13.
- Wurz, P., Rohner, U., Whitby, J.A., Kolb, C., Lammer, H., Dobnikar, P., Martín-Fernández, J.A., 2007. The lunar exosphere: The sputtering contribution. *Icarus* 191, 486–496.
- Wurz, P., Whitby, J.A., Rohner, U., Martín-Fernández, J.A., Lammer, H., Kolb, C., 2010. Self-consistent modelling of Mercury's exosphere by sputtering, micro-meteorite impact and photon-stimulated desorption. *Planet. Space Sci.* 58, 1599–1616.
- Ziegler, J.F., 2004. SRIM-2003. *Nucl. Instrum. Methods Phys. Res. Sect. B: Beam Interact. Mater. At.* 219–220, 1027–1036.
- Ziegler, J.F., Biersack, J.P., Littmark, U., 1984. *The Stopping and Range of Ions in Solids. Stopping and Ranges of Ions in Matter*. vol. 1. Pergamon Press, New York.
- Ziegler, J.F., Biersack, J.P., Ziegler, M.D., 2013. <http://www.srim.org> URL checked on 2014/01/13.